

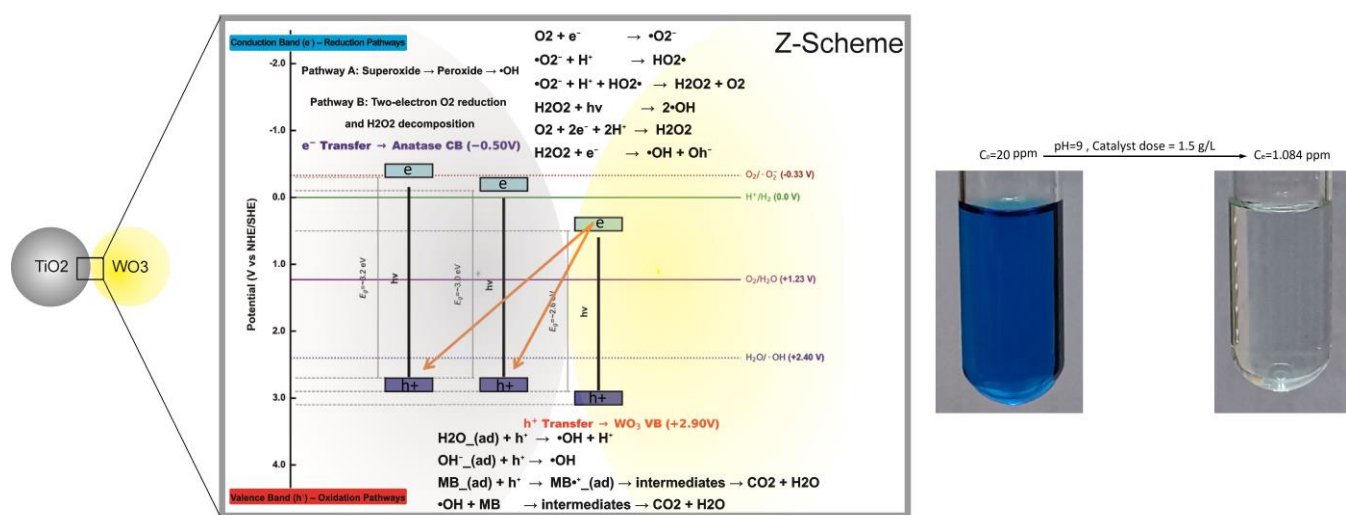
# Green synthesized $\text{TiO}_2\text{-P25/WO}_3$ photocatalyst for methylene blue degradation under sunlight in a spherical reactor

Mahdi Jamshidi<sup>1</sup> , Ali Amoozadeh<sup>2,\*</sup> 

<sup>1</sup>Department of Applied Chemistry, Faculty of Chemistry, Semnan University, Semnan, Iran.

<sup>2</sup>Department of Organic Chemistry, Faculty of Chemistry, Semnan University, Semnan, Iran.

## GRAPHICAL ABSTRACT



## ARTICLE INFO

### Article type:

Research Article

### Article history:

Received xx Month xxx

Received in revised form xx Month xxx

Accepted xx Month xxx

Available online x Month xx

### Keywords:

Photocatalysis

$\text{TiO}_2\text{-P25}$

Central composite design

Sunlight irradiation

Methylene blue



© The Author(s)

Publisher: Razi University

## ABSTRACT

Nanostructured semiconductors have emerged as promising photocatalysts for sustainable wastewater purification. Among them,  $\text{TiO}_2\text{-P25}$  (commercial  $\text{TiO}_2$ ) is widely used; however, its wide band gap restricts visible light activity. A simple and eco friendly approach to overcome this limitation is the formation of heterostructures. In this work,  $\text{TiO}_2\text{-P25/WO}_3$  heterostructures were synthesized via a rapid, additive free aqueous sonochemical route (10 min ultrasonication). The structural characteristics of the composites were examined by XRD, FTIR, Raman spectroscopy and FESEM, while their optical and interfacial properties were assessed by DRS,  $\zeta$  potential and EIS analyses. These characterizations confirmed that the anatase-rutile  $\text{TiO}_2\text{-P25}$  and monoclinic  $\text{WO}_3$  phases remained intact without the appearance of new interfacial bonds, while close physical contact between the two oxides improved visible light absorption and facilitated interfacial charge transfer. The photocatalytic performance was evaluated in a spherical quartz reactor under real sunlight using methylene blue (MB) as a model pollutant. Response surface methodology with a central composite design was employed to investigate the effects of catalyst dose (0.5–1.5 mg/L), initial MB concentration (20–40 mg/L), and pH (5–9). Under the optimized conditions (20 mg/L MB, 1.5 mg/L catalyst, pH 9), 69.5% of MB was removed by dark adsorption within 30 min, and subsequent sunlight irradiation resulted in 94.6% total removal after 70 min, with a reaction rate constant of  $0.042 \text{ min}^{-1}$ . Taken together, these results demonstrate that this simple aqueous synthesis provides an efficient and eco friendly pathway to prepare  $\text{TiO}_2\text{-P25/WO}_3$  photocatalysts for large scale wastewater remediation under real sunlight.

## 1. Introduction

Water pollution originating from industrial effluents—particularly from textile, paper, leather, cosmetic, and food industries—remains a major environmental concern due to the persistence, toxicity, and bioaccumulation potential of synthetic dyes (Khan *et al.* 2022; Khan *et al.* 2024).

\*Corresponding author Email: [aamoozadeh@semnan.ac.ir](mailto:aamoozadeh@semnan.ac.ir)

Among these contaminants, methylene blue (MB) is one of the most frequently used cationic dyes and is known for its high stability, low biodegradability, and strong chromatic intensity, which reduce light penetration and adversely affect aquatic ecosystems. (Gonzalez and Jaramillo-Fierro 2025; Kalaycioglu *et al.* 2023; Khan *et al.* 2022)

Conventional wastewater treatment methods, such as adsorption,

coagulation–flocculation, membrane filtration, and biological treatment, often fail to achieve complete mineralization and may lead to secondary waste generation or high operational costs, highlighting the need for sustainable and energy-efficient alternatives based on renewable energy inputs. (Balu *et al.* 2024; Khan *et al.* 2022; Khatami and Iravani 2021; Liu *et al.* 2020) Heterogeneous photocatalysis has emerged as a promising technology for the degradation of persistent organic pollutants through light-driven generation of reactive oxygen species. Titanium dioxide ( $\text{TiO}_2$ ) is a benchmark photocatalyst because of its chemical stability, low toxicity, and strong oxidative potential, yet its relatively wide band gap (3.0–3.2 eV) limits absorption primarily to ultraviolet light, which accounts for only a small fraction of the solar spectrum. (Al-Ghamdi *et al.* 2025; Azeez *et al.* 2018; Farghaly *et al.* 2024; Yin, Liu and Ai 2021) Conversely, tungsten trioxide ( $\text{WO}_3$ ), with a narrower band gap (2.4–2.8 eV), exhibits efficient visible-light absorption but suffers from a conduction band potential that is insufficient for effective reduction reactions. Integrating  $\text{TiO}_2$  with  $\text{WO}_3$  to form a heterojunction structure can synergistically enhance light harvesting, charge separation, and redox selectivity, thereby improving overall photocatalytic performance. (González Rodríguez *et al.* 2020; 2019; Liu *et al.* 2020; Yang *et al.* 2025) Extensive spectroscopic and electrochemical studies have revealed that the charge transfer mechanisms in  $\text{TiO}_2$ – $\text{WO}_3$  composites depend strongly on the interface quality and band alignment, exhibiting either type-II or Z-scheme behavior depending on structural and electronic factors.) Azeez *et al.* 2018; Matinise *et al.* 2025) Therefore, precise interface engineering is crucial for achieving efficient charge transfer and broad-spectrum sunlight utilization. However, most reported synthesis routes—such as hydrothermal, sol–gel, or solvothermal methods—require organic solvents, oxidants, and high-temperature calcination, which are energy-intensive and often inconsistent with the principles of green chemistry (Hosseini, Amoozadeh and Akbarzadeh 2019; Hou and Hao 2021; Moghni *et al.* 2022; Nik Fatin Nabihah Atiqah Nik Ramli *et al.* 2024). According to the framework proposed by Anastas and Warner (1998), green chemistry promotes the design of chemical products and processes that minimize or eliminate hazardous substances through the use of benign solvents, renewable feedstocks, energy efficiency, and waste prevention (Anastas and Warner 2000).

Recent studies have demonstrated that sonochemical and wet-chemical routes can effectively produce  $\text{TiO}_2$ / $\text{WO}_3$ -based photocatalysts through energy-efficient and environmentally benign processes. Ernowati *et al.* (2019) synthesized mesoporous  $\text{WO}_3$ / $\text{TiO}_2$  nanocomposites using water as a dispersion medium and mild drying at 80 °C, achieving up to 96% degradation of methylene blue within 120 min under UV irradiation due to enhanced surface area and defect sites. Moghni *et al.* (2022) employed a combined sonochemical–microwave method to prepare  $\text{TiO}_2$ / $\text{WO}_3$  nanocomposites that exhibited improved charge separation, extended light absorption, and stable reusability under both UV and solar light irradiation. Cheng *et al.* (2023) reported W– $\text{TiO}_2$  nanopowders synthesized via a sol–gel route, where adsorption and photocatalysis acted synergistically to enhance methylene blue removal under sunlight, confirming visible-light activation. In addition, Głowniak *et al.* (2023) reviewed the broader role of ultrasound-assisted synthesis as a green and energy-saving approach that promotes rapid reactions in aqueous systems with reduced waste and high product efficiency. Collectively, these findings demonstrate that combining aqueous media, ultrasonic or low-temperature activation, and sunlight utilization aligns well with the principles of green chemistry and offers a sustainable route for  $\text{TiO}_2$ / $\text{WO}_3$  photocatalyst fabrication. (Cheng *et al.* 2024; Głowniak *et al.* 2023; L. Ernowati *et al.* 2019; Moghni *et al.* 2022) Building upon these insights, this study developed a simple aqueous sonochemical route for synthesizing  $\text{TiO}_2$ –P25/ $\text{WO}_3$  nanocomposites. Water was used as a safe and renewable solvent, and short-wave ultrasound facilitated close contact between the nanoparticles under ambient conditions, avoiding organic reagents or post-calcination. The photocatalytic performance was evaluated under natural sunlight, serving as a clean and renewable energy source. This straightforward process aligns with the twelve principles of green chemistry, offering an environmentally sound and easily scalable strategy for sustainable water purification.

## 2. Materials and methods

### 2.1. Synthesis of $\text{TiO}_2$ –P25/ $\text{WO}_3$ (Ultrasonication-assisted physical mixing)

Titanium dioxide ( $\text{TiO}_2$ –P25, Evonik; ca. 20–40 nm; anatase/rutile  $\approx$  3:1) and tungsten oxide ( $\text{WO}_3$ , US Nano, USA; monoclinic phase) were used as received. Methylene blue (MB) (analytical grade, Merck) served as the model dye. Sodium hydroxide (NaOH,  $\geq 98\%$ ) and

hydrochloric acid (HCl, 1 M) were used to adjust the solution pH. All aqueous solutions were prepared with deionized water (18.2 M $\Omega$ ·cm). A  $\text{TiO}_2$ –P25/ $\text{WO}_3$  composite containing 30 wt.%  $\text{WO}_3$  relative to  $\text{TiO}_2$ –P25 (hereafter referred to as TW) was synthesized via a mild, aqueous, additive-free sonochemical route. The 30 wt.%  $\text{WO}_3$  loading was selected based on literature-reported optimization ranges (typically 25–30 wt.%) for  $\text{TiO}_2$ / $\text{WO}_3$  systems targeting methylene blue degradation, ensuring efficient charge separation and visible-light absorption (L. Ernowati *et al.* 2019). In a typical procedure, 1.00 g of  $\text{TiO}_2$ –P25 and 0.30 g of  $\text{WO}_3$  were co-dispersed in 50 mL of deionized water under magnetic stirring (400 rpm, 15 min). The suspension was then subjected to ultrasonic irradiation (40 kHz, 150 W) for 10 min at ambient temperature ( $25 \pm 2$  °C). The resulting slurry was dried in an oven at 80 °C for 12 h, gently ground in an agate mortar, and sieved (<200 mesh) to obtain a uniform powder. This low-temperature, scalable, and physical processing route was designed to preserve the crystalline structures of both oxides while promoting intimate interfacial contact within the  $\text{TiO}_2$ – $\text{WO}_3$  heterojunction, consistent with the principles of green chemistry.

X-ray diffraction (XRD) patterns were collected on a Bruker D8 Advance diffractometer (Cu K $\alpha$ ,  $\lambda = 1.5406$  Å; 40 kV, 30 mA;  $2\theta$  range 10–80°). Fourier-transform infrared (FTIR) spectra were recorded on a Thermo Nicolet iS10 (400–4000  $\text{cm}^{-1}$ ; KBr pellet). Raman spectra were measured using a Horiba Jobin Yvon LabRAM HR spectrometer (532 nm excitation). UV–Vis diffuse reflectance spectra (DRS) were acquired on a Shimadzu UV-2600 using  $\text{BaSO}_4$  as the reference. Electrochemical impedance spectroscopy (EIS) was performed with a Metrohm Autolab PGSTAT302N potentiostat over 0.1 Hz–100 kHz with a 10 mV AC perturbation. Morphology and elemental composition were examined by FESEM (Hitachi S-4800) operated at 10 kV after Au sputter-coating.

For the photocatalytic experiments, solids were separated using a Universal centrifuge (Sabalan Azim Tabriz, Iran) at 4000 rpm for 10 min. Solution pH was adjusted and monitored using a digital pH meter (Lutron PTR-79, Taiwan). Ultrasonication during sample preparation was carried out in an ultrasonic bath (Backer VClean, 40 kHz, 150 W). Dye concentrations were monitored by a UV–Vis spectrophotometer (Jenway 6200, UK).

### 2.2. photocatalytic experiment

Photocatalytic degradation of methylene blue (MB) was carried out in a spherical batch reactor modified from a round-bottom flask (quartz, working volume 250 mL). Experiments were performed outdoors in Kermanshah, Iran, from April to June 2025, within a fixed solar window (11:00–15:00 local time) under clear-sky conditions (ambient temperature 25–30 °C). Fresh MB solutions at the prescribed initial concentrations were introduced into the reactor; a fixed amount of catalyst was then added, and the suspension was magnetically stirred to ensure homogeneity. The solution pH was adjusted to the target value using dilute HCl or NaOH. Prior to irradiation, the mixture was kept in the dark for 30 min to establish adsorption–desorption equilibrium. Global solar irradiance was tracked with a handheld solar meter and was typically  $\sim 600$ –800  $\text{W m}^{-2}$  during the testing window.

To control for non-photocatalytic pathways, three parallel controls were run: dark adsorption (catalyst + dark), photolysis (MB + light, no catalyst), and catalyst in the dark. At predetermined intervals, aliquots were withdrawn, immediately shielded from light, and centrifuged (4000 rpm, 10 min) to remove suspended solids. The clarified supernatant was measured on a Jenway 6200 UV–Vis spectrophotometer (1 cm cuvette) at 664 nm using a multi-point calibration curve; MB removal was computed as  $100 \times (1 - C_t/C_0)$ . For kinetic analysis, the apparent pseudo-first-order rate constant  $k_{\text{app}}$  was obtained from linear fits of  $\ln(C_0/C_t)$  versus time. Each condition was tested in triplicate, and results are reported as mean  $\pm$  SD to ensure reproducibility.

$$\text{Removal (\%)} = 100 \times (1 - C_t/C_0) \quad (1)$$

$$\ln(C_0/C_t) \text{ vs. time} \rightarrow \text{slope} = k_{\text{app}} \quad (2)$$

### 2.3. Design of experiments and data analysis (RSM/CCD)

A rotatable central composite design (CCD) with three factors—initial MB concentration, mg/L (A), catalyst dose, g/L (B), and solution pH (C)—was employed to quantify individual and interaction effects. Rotatability was achieved with  $\alpha \approx 1.68$  (coded levels  $-\alpha, -1, 0, +1, +\alpha$ ). Accordingly, the actual factor levels extended beyond the central factorial bounds, as follows (center  $\pm$  step in parentheses): Initial MB concentration, mg/L (A): 13.182 ( $-\alpha$ ), 20 ( $-1$ ), 30 (0), 40 ( $+1$ ), 46.818 ( $+\alpha$ ) (center  $30 \pm 10$ )

Catalyst dose, g/L(B): 0.5 (−1), 1.0 (0), 1.5 (+1), 1.8409 (+α); the lower axial level (0.159 g/L) implied by rotatability was constrained to 0.5 g/L for practicality and suspension stability. (center  $1.0 \pm 0.5$ )

pH (C): 3.636 (−α), 5 (−1), 7 (0), 9 (+1), 10.364 (+α) (center  $7 \pm 2$ )

The design comprised 16 runs (full factorial + axial) with randomized run order and was augmented with confirmation experiments (neat  $\text{TiO}_2$ -P25, neat  $\text{WO}_3$ , and photolysis). The response (Removal (%)) was modeled by a second-order polynomial, and ANOVA (model F, p-values,  $R^2$ ,  $R^2_{\text{adj}}$ ,  $R^2_{\text{pred}}$ , PRESS, Adeq. Precision) as well as lack-of-fit tests were used to assess adequacy. Residual diagnostics (normality and homoscedasticity) were examined prior to optimization.

### 3. Result and discussion

#### 3.1 Characterization

To determine the crystal structure of the nanoparticles, X-ray diffraction XRD was recorded and the results are shown in Fig. 1.  $\text{TiO}_2$ -P25 consists of anatase and rutile phases; for  $\text{TiO}_2$ -P25, the peaks at  $25.3^\circ$  (101, anatase) and  $27.4^\circ$  (110, rutile) are characteristic. In Fig. 1(c), monoclinic  $\text{WO}_3$  exhibits reflections at  $23.1^\circ$  (002),  $23.7^\circ$  (020),  $24.2^\circ$  (200) and  $34.1^\circ$  (202) (JCPDS 43-1035). The diffraction pattern of the composite [Fig. 1(b)] essentially conforms to  $\text{TiO}_2$ -P25 with a discernible trace of  $\text{WO}_3$ ; the intensity of  $\text{WO}_3$  reflections decreases as its fraction is reduced. Accordingly, the simultaneous presence of  $\text{TiO}_2$ -P25 and  $\text{WO}_3$  reflections without extra peaks indicates phase co-existence and supports a physical  $\text{TiO}_2$ -P25/ $\text{WO}_3$  heterostructure with preserved crystallinity (Sotelo-Vazquez *et al.* 2017).

Low-magnification FESEM images (Fig. 2a for  $\text{TiO}_2$ -P25; Fig. 2b for  $\text{TiO}_2$ -P25/ $\text{WO}_3$ ) show agglomerated clusters with a fairly uniform particle distribution and no visible cracks or voids, as commonly reported for oxide nanopowders (Boga *et al.* 2018; Serra-Pérez *et al.* 2024). For  $\text{TiO}_2$ -P25, aggregate-size statistics obtained from  $n = 140$  objects at 20 kx (analyzed in ImageJ using thresholding and the Feret diameter) yielded a mean  $\pm$  SD of  $188 \pm 215$  nm with a median of  $\sim 89$  nm, indicating a strongly right-skewed distribution due to aggregation (Nguyen *et al.* 2024; Sotelo-Vazquez *et al.* 2017). At higher magnification (200 kx), both  $\text{TiO}_2$ -P25 and the physical  $\text{TiO}_2$ -P25/ $\text{WO}_3$

mixture display near-spherical primary nanoparticles in the  $\sim 20$ – $60$  nm range, in agreement with literature values for  $\text{TiO}_2$ -P25 (20–40 nm) and  $\text{TiO}_2$ -P25/ $\text{WO}_3$  composites ( $\sim 28$ – $60$  nm) (Boga *et al.* 2018; Hosseini, Amoozadeh and Akbarzadeh 2019). The images therefore, support a hierarchical texture, where primary nanocrystallites assemble into larger secondary aggregates (Min *et al.* 2025; Nguyen *et al.* 2024). In the physical mixture, the  $\text{TiO}_2$ -P25/ $\text{WO}_3$  contact appears predominantly interfacial (physical); together with FTIR/Raman showing no new interfacial bands, this is consistent with a non-grafted physical heterostructure rather than chemical integration (Dolatyari *et al.* 2024; Sotelo-Vazquez *et al.* 2017).

The FTIR profiles of  $\text{TiO}_2$ -P25,  $\text{WO}_3$ , and their physical mixture show an additive superposition of the constituents' fingerprints.  $\text{TiO}_2$ -P25 presents the broad lattice Ti–O/Ti–O–Ti envelope below  $1000$   $\text{cm}^{-1}$ , together with surface-hydroxyl bands at  $\sim 1623$  and  $\sim 3355$   $\text{cm}^{-1}$ .  $\text{WO}_3$  exhibits W–O–W stretching in the  $\sim 777$ – $838$   $\text{cm}^{-1}$  region and O–H/H–O–H modes at  $\sim 1629$  and  $3400$ – $3500$   $\text{cm}^{-1}$ , indicative of surface-adsorbed water. The composite retains these features without additional bands, consistent with a simple physical mixture lacking new interfacial vibrations; this "spectral superposition" behavior agrees with prior  $\text{TiO}_2$ -P25/ $\text{WO}_3$  reports (Boga *et al.* 2018). Notably, covalently linked systems (e.g., ECH-bridged  $\text{TiO}_2$ -P25– $\text{WO}_3$ ) introduce organic absorptions (C–H  $\sim 2780$ – $2930$   $\text{cm}^{-1}$ ; C–O–C  $\sim 1265$   $\text{cm}^{-1}$ ), which are absent here, supporting a non-grafted composite (Kulkarni *et al.* 2025).

Pristine anatase  $\text{TiO}_2$ -P25 (Fig. 4a) exhibits characteristic Raman modes at  $\sim 147$ ,  $398$ ,  $517$ , and  $641$   $\text{cm}^{-1}$ , in agreement with earlier reports (Kanafin *et al.* 2025; Kulkarni *et al.* 2025).  $\text{WO}_3$  (Fig. 4b) shows its well-documented bands at  $\sim 271$   $\text{cm}^{-1}$  (O–W–O bending) and at  $\sim 716$  and  $807$   $\text{cm}^{-1}$  (bridging W–O–W stretching). The spectrum of the mechanically mixed  $\text{TiO}_2$ -P25/ $\text{WO}_3$  sample (Fig. 4c) is essentially a straightforward superposition of these two sets of modes, without the appearance of additional peaks, confirming that mechanical mixing does not induce the formation of new Raman-active phases (Boga *et al.* 2018; Tran *et al.* 2019). Only slight peak shifts ( $\leq 2$   $\text{cm}^{-1}$ ) are detected, which are typically explained by local strain or weak electrostatic perturbations at particle–particle interfaces (Bhavani *et al.* 2022; Li *et al.* 2025).

#### XRD peaks (assigned, only) – stricter rules + shift-scan for MIX

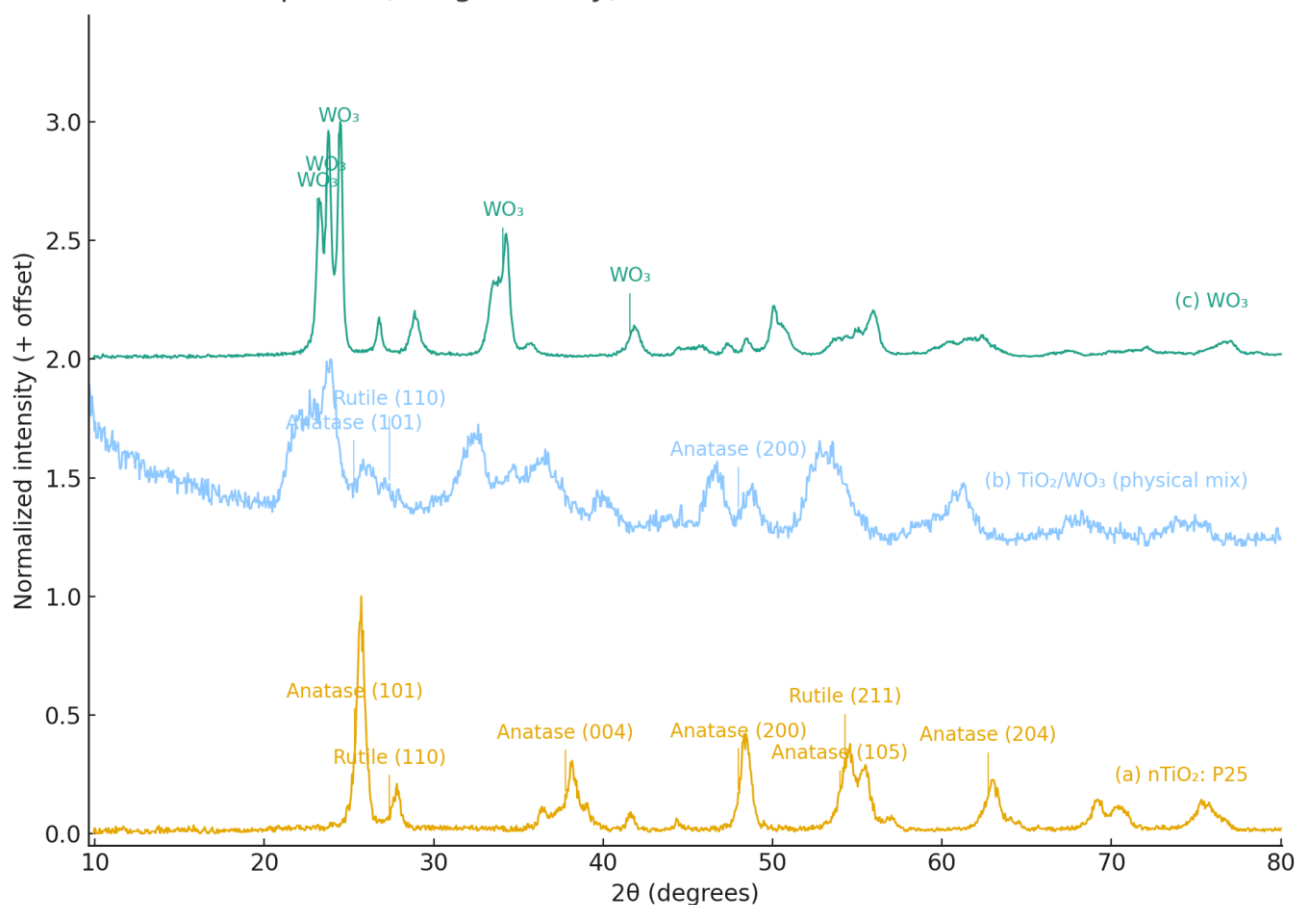


**Fig. 1.** XRD patterns of (a) n- $\text{TiO}_2$ -P25-, (b)  $\text{TiO}_2$ -P25/ $\text{WO}_3$  physical mixture, and (c)  $\text{WO}_3$ .  $\text{TiO}_2$ -P25 shows anatase with minor rutile; the composite displays  $\text{WO}_3$  reflections, confirming coexistence of both oxides without extraneous peaks.

DRS (UV–vis diffuse reflectance) Diffuse reflectance was converted via the Kubelka–Munk function and optical band gaps were estimated using Tauc plots with the appropriate transition exponents. Pristine  $\text{TiO}_2$ -P25 (Fig. 5a) shows a direct allowed transition with  $E_g = 3.21$  eV, in excellent agreement with the canonical 3.0–3.2 eV range for Degussa  $\text{TiO}_2$ -P25. Monoclinic  $\text{WO}_3$  (Fig. 5b) exhibits an indirect transition with  $E_g = 2.53$  eV after mild baseline correction, although slightly below the typical 2.6–2.8 eV window (Boga *et al.* 2018; Sotelo-Vazquez *et al.* 2017), such a modest redshift falls within reported variability and can arise from morphology-dependent electronic structure or surface states (Yan *et al.* 2020). The  $\text{TiO}_2$ -P25/ $\text{WO}_3$  physical mixture (TW) (Fig. 5c) displays a direct apparent gap of  $E_g = 2.97$  eV intermediate between the parent oxides—consistent with optical coupling/superposition in  $\text{TiO}_2$ -P25/ $\text{WO}_3$  composites, where the absorption edge extends slightly into the visible while retaining features

of the constituents (Sotelo-Vazquez *et al.* 2017; Yang *et al.* 2025). To extract these values, diffuse reflectance ( $R^\infty$ ), referenced to  $\text{BaSO}_4$ , was transformed to a pseudo-absorbance using the Kubelka–Munk relation:

$$F(R^\infty) = (1 - R^\infty)^2 / (2R^\infty) \quad (3)$$

Optical band gaps were determined from Tauc plots by extrapolating the linear portion of  $(F(R^\infty) hv)^n$  versus  $hv$ :

$$(F(R^\infty) hv)^n = A (hv - E_g) \quad (4)$$

where  $hv$  is the photon energy,  $A$  is a proportionality constant, and  $n$  depends on the transition type:  $n = 2$  for direct allowed transitions (applied to  $\text{TiO}_2$ -P25) and  $n = 1/2$  for indirect allowed transitions (applied to monoclinic  $\text{WO}_3$ ).

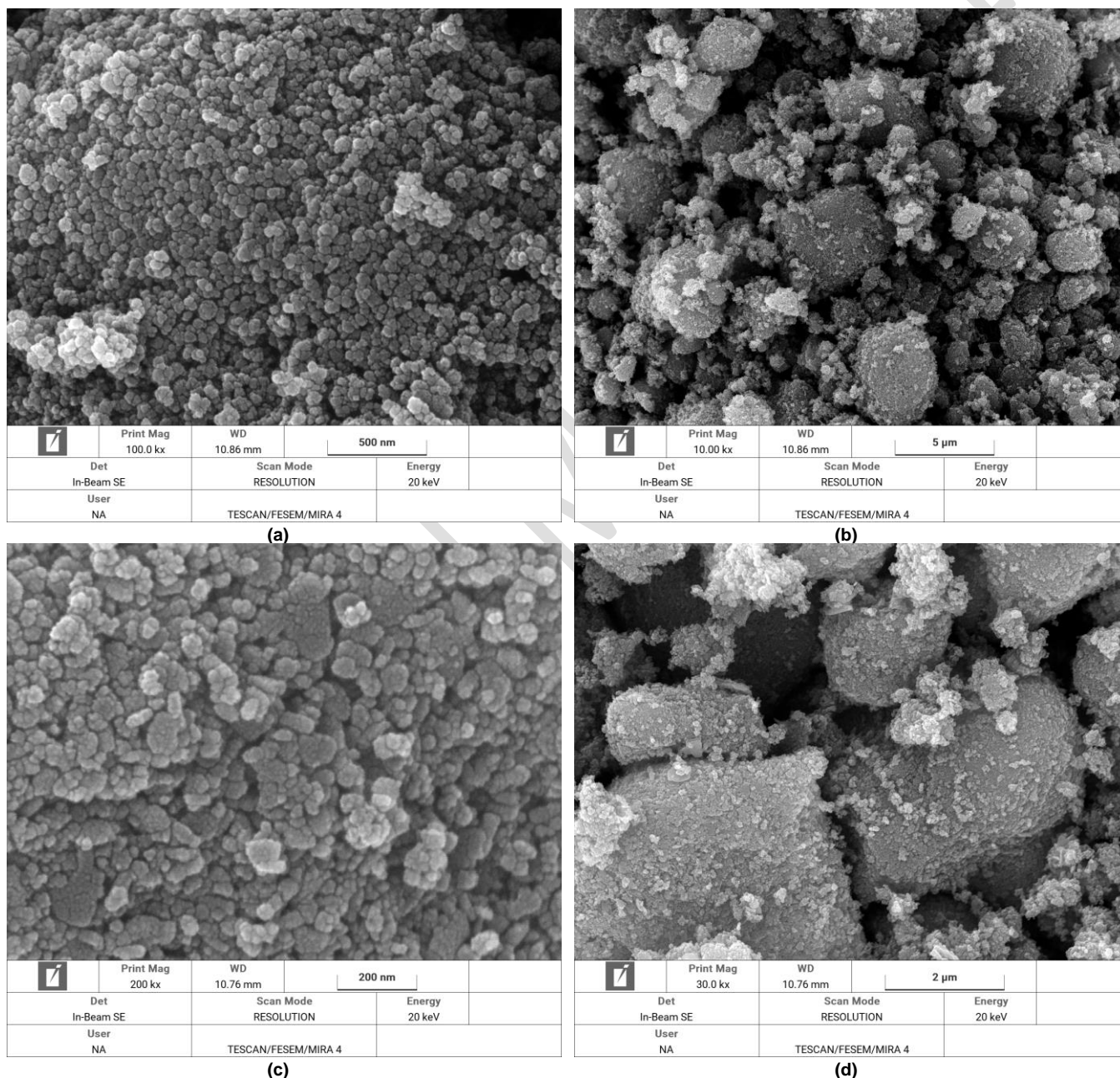


**Fig. 2.** FESEM images of (a)  $\text{TiO}_2$ -P25 and (b)  $\text{TiO}_2$ -P25/ $\text{WO}_3$  composite. Both display nearly spherical to ellipsoidal particles of ~20–40 nm, with evident agglomeration more pronounced in the composite.

### 3.2. Photocatalytic performance

Under identical sunlight and a 30-minute dark equilibration, the physically mixed  $\text{TiO}_2$ -P25/ $\text{WO}_3$  composite (TW) consistently outperforms the single oxides (T and W) in methylene-blue removal across the compiled time-profiles and panel summaries (Hou and Hao 2021; Sharifiyan, Fattah-alhosseini and Karbasi 2023). Control comparisons resolve contributions: photolysis is minor, T is moderately photoactive, and W shows the strongest dark-phase uptake yet lower

net photoactivity—exactly the pattern visible in the TW/TW/Photolysis panel of Fig. 7  $\text{WO}_3$ 's larger dark adsorption relative to  $\text{TiO}_2$ -P25 is consistent with electrostatic attraction of cationic MB to more negative surfaces near neutral pH, supported by the measured zeta potential (−22.4 mV), the low isoelectric point (IEP) of  $\text{WO}_3$ , and the point-of-zero-charge ( $\text{pH}_{\text{PZC}}$ )/charge-controlled uptake arguments (Ahmadpour *et al.* 2024; Bollinger *et al.* 2025). The catalyst-dose panel exhibits the classical optimum: performance rises with loading and then levels off/declines as light scattering/screening and particle aggregation curb



effective photon use (Bollinger *et al.* 2025). DLS (peak  $\approx 245.6$  nm; PI  $\approx 0.94$ ) corroborates partial aggregation in suspension, rationalizing the high-loading plateau in the dose dependence (Bollinger *et al.* 2025). Increasing the initial MB concentration depresses apparent removal via inner-filter (Beer–Lambert) and active-site saturation effects, consistent with the concentration-panel trends (Bollinger *et al.* 2025; Vasiljevic *et al.* 2020). Activity increases toward mildly alkaline pH, aligning with stronger attraction of cationic MB to negatively charged surfaces and with facilitated hydroxyl-radical ( $\cdot\text{OH}$ ) formation under irradiation. Light-stage kinetics follow a pseudo-first-order model,  $\ln(C_0/C) = k_{\text{app}} t$ , with  $k_{\text{app}}(\text{TW}) > k_{\text{app}}(\text{T}) \gg k_{\text{app}}(\text{photolysis})$ , matching the slope hierarchy in the kinetics panel (Bollinger *et al.* 2025; Shoaib *et al.* 2023). Complementarily, EIS (Nyquist) exhibits a smaller arc and lower

charge-transfer resistance ( $R_{\text{ct}}$ ) for TW than for T (Fig. 6), indicating facilitated interfacial charge transport at the Ti–W contact—coherently explaining the superior  $k_{\text{app}}$  and total removal of TW (Hou and Hao 2021; Sharifiyan, Fattah-alhosseini and Karbasi 2023). Taken together, Fig. 7 supports a cooperative scenario in which W pre-concentrates MB in the dark, while T drives faster photo-turnover upon illumination, delivering the best overall performance for TW under the tested conditions (Sharifiyan, Fattah-alhosseini and Karbasi 2023). To quantify and generalize these trends, we developed an RSM model (ANOVA, parity plots, and response surfaces; Fig. 8, Table 1–2) and identified an operating optimum, which was validated by confirmation runs.

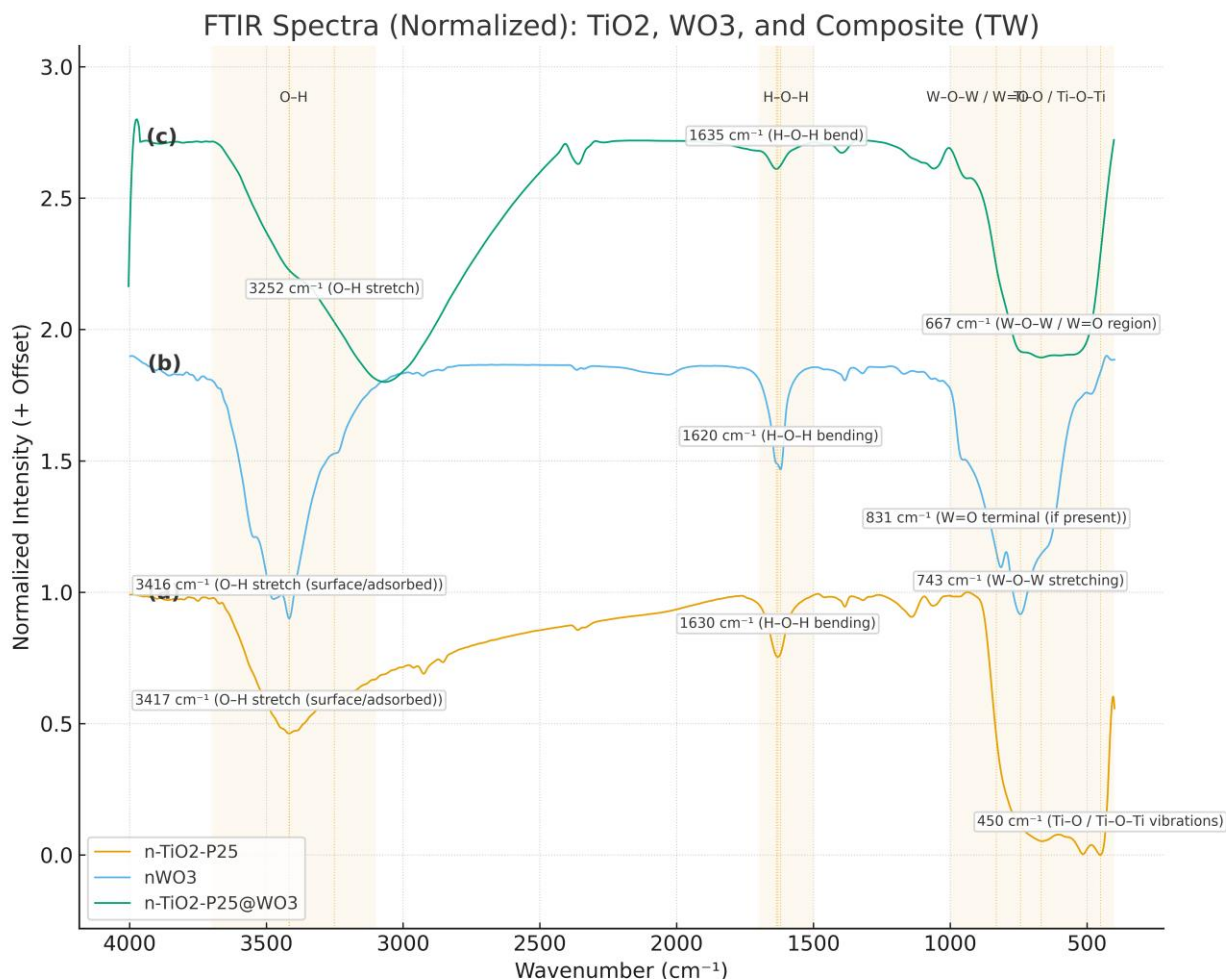


**Fig. 3.** FTIR spectra of (a)  $\text{TiO}_2$ -P25 (b)  $\text{WO}_3$ , and (c)  $\text{TiO}_2$ -P25/ $\text{WO}_3$  composite. The composite resembles a superposition of the parent spectra, showing no new absorption bands or significant shifts.

Photocatalytic tests under identical conditions showed higher removal for TW than T (Fig. 7); pseudo-first-order fits,  $\ln(C_0/C) = k \cdot t$ , gave  $k_{\text{T}}$  for T and  $k_{\text{TW}}$  for TW (Fig. 7). The contracted Nyquist arc of TW (Fig. 6) reveals lower  $R_{\text{ct}}$  and more efficient interfacial charge transport across the Ti–W contact. This behavior is consistent with previous reports that faster interfacial transfer prolongs effective carrier lifetimes (Ghiloufi *et al.* 2024; Sotelo-Vazquez *et al.* 2017). In our physically contacted system, the reduced  $R_{\text{ct}}$  is sufficient to account for the improved  $k_{\text{app}}$  and overall removal, without invoking covalent linking. Consequently, the EIS results support a mechanism of efficient charge separation and interfacial transport compatible with a physical Ti–W heterostructure. As shown in Table 1, several representative studies are compared with our work for a direct performance benchmark.

### 3.3. RSM/DOE modeling & optimization

The ANOVA summary (Table 1) indicates that the quadratic response surface for Removal Efficiency is statistically robust and practically meaningful. The model achieved an overall F-value of 15.81 ( $p = 0.0007$ ), with a non-significant lack-of-fit ( $p = 0.0614$ ) and strong indicators of model quality ( $R^2 = 0.9531$ ,  $\text{adj-}R^2 = 0.8928$ ,  $\text{pred-}R^2 = 0.4543$ ,  $\text{Adeq. Precision} = 12.75$ ). These results support the adequacy of the model for prediction and optimization. However, the relatively

large gap between predicted and adjusted  $R^2$  suggests that model reduction, response transformation, or confirmatory runs may be beneficial.

Model diagnostics shown in Fig. 8 further reinforce this conclusion. The normal probability plot of externally studentized residuals (Fig. 8a) follows the reference line closely, confirming approximate normality of the residuals. The residuals vs. predicted plot (Fig. 8b) exhibits a random scatter around zero, with no evident trends or funneling, indicating homoscedastic variance and no dominant outliers, although a few influential points are noted in the diagnostics table. The 3D response surface (Fig. 8c) illustrates clear curvature: increasing catalyst dose (B) improves removal efficiency but with diminishing returns, while higher initial dye concentration (A) decreases performance. This interaction defines an interior operating optimum, visible in both the surface and contour plots. Finally, the parity plot (Fig. 8d) demonstrates predictive validity, as the data points cluster near the  $45^\circ$  line with a slope close to unity, consistent with the high  $R^2$  values and the non-significant lack-of-fit in Table 1. In summary, both the statistical metrics and graphical diagnostics point to the same conclusion: the CCD/RSM model is well-behaved and reliable, displaying the hallmarks of a robust quadratic fit—clear curvature, adequate signal-to-noise ratio, and strong agreement between predicted and experimental responses.

$$Y = \beta_0 + \sum \beta_i x_i + \sum \beta_{ii} x_i^2 + \sum \beta_{ij} x_i x_j \quad (5)$$

The quadratic model for Removal Efficiency (Y) expressed in terms of coded factors is:

$$Y = 75.08 - 3.14A + 5.09B + 6.94C + 3.22AB - 0.12AC - 2.18BC + 3.83A^2 + 2.34B^2 + 0.97C^2 \quad (6)$$

where A represents the initial dye concentration, B the catalyst dose, and C the pH. This coded equation can be used to predict the response

within the experimental range, where the low and high levels of each factor are coded as  $-1$  and  $+1$ , respectively. The coefficient magnitudes highlight the relative impact of each term: the positive linear effects of catalyst dose (B) and pH (C) dominate, while dye concentration (A) contributes negatively. The interaction between A and B is positive, whereas the interaction between B and C is negative. The quadratic terms ( $A^2$ ,  $B^2$ ,  $C^2$ ) capture curvature in the response surface. Overall, this regression model quantifies the combined influences of the three factors and supports the identification of optimal operating conditions.

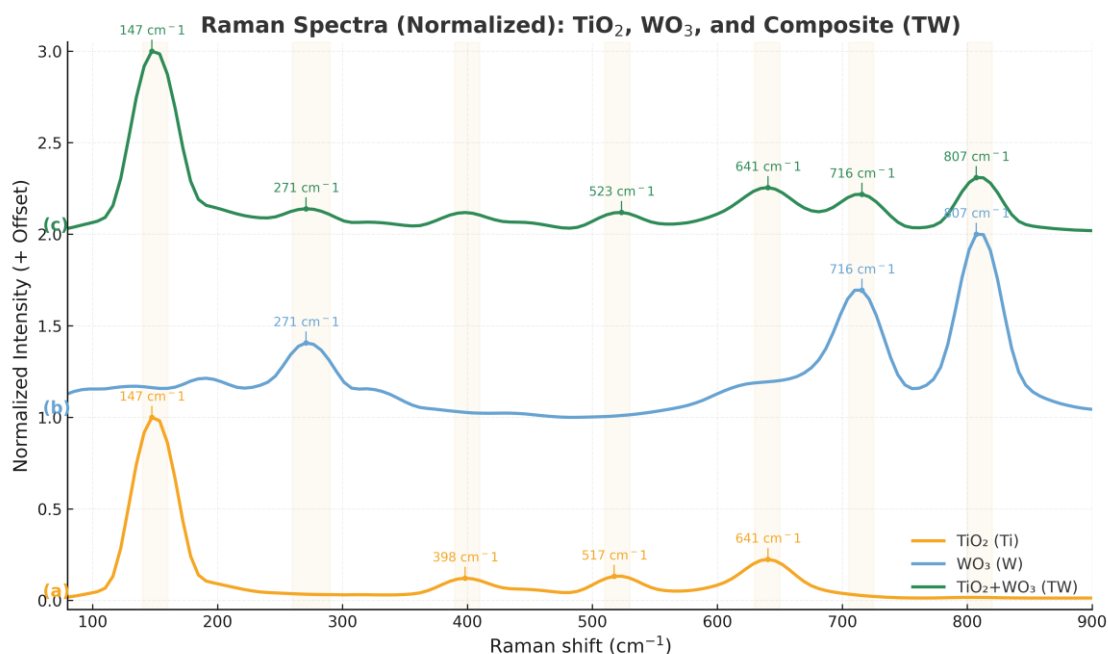


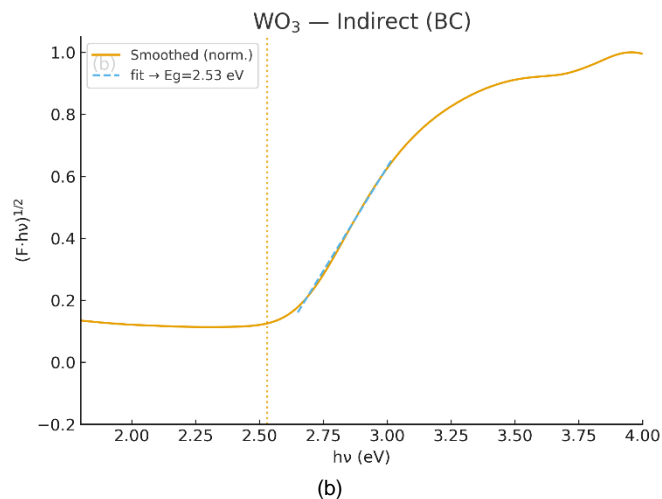
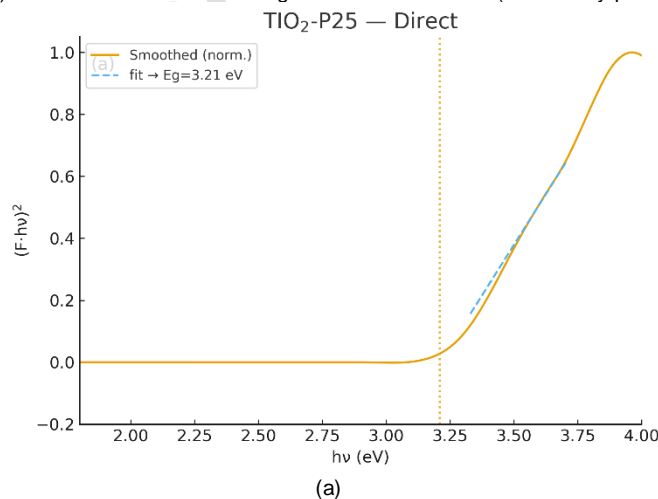
**Fig. 4.** Raman spectra of (a)  $\text{TiO}_2$ -P25, (b)  $\text{WO}_3$ , and (c)  $\text{TiO}_2$ -P25/ $\text{WO}_3$  composite. Characteristic modes of both oxides are retained without new peaks or marked shifts, consistent with a physical rather than grafted interface.

### 3.4. Mechanism

Under real sunlight, both  $\text{TiO}_2$ -P25 and  $\text{WO}_3$  generate electron-hole pairs, and their fate is governed by band alignment and the nature of the interfacial contact. In this physically mixed nanocomposite, close particle-particle contact enables charge redistribution between adjacent particles without introducing new chemical bonds or defects. Although non-covalent, such interfaces can still drive efficient charge separation by providing a driving force for carrier transfer across the contact, consistent with type-II or direct Z-scheme-like behavior. Keeping the crystal lattices intact while allowing short-range coupling—often discussed for closely contacted oxide composites—helps preserve strong redox activity and limit recombination, which is crucial for solar photocatalysis (Brandl *et al.* 2020; Serpone and Emeline 2012). In line with this picture, electrochemical impedance spectroscopy (Fig. 6) shows a reduced TW charge-transfer resistance (smaller Nyquist

feature), indicating the formation of an interfacial electron-transport channel. (Park *et al.* 2016; Sotelo-Vazquez *et al.* 2017).

In the physically contacted  $\text{TiO}_2$ -P25/ $\text{WO}_3$  composites, interfacial charge annihilation occurs through the recombination of weak electrons from  $\text{WO}_3$  with weak holes in  $\text{TiO}_2$ , forming a Z-scheme charge-transfer pathway. As a result, the strong electrons accumulate on  $\text{TiO}_2$ -P25 and reduce adsorbed  $\text{O}_2$  to generate reactive oxygen species ( $\cdot\text{O}_2^-$ ,  $\text{HO}_2^\cdot$ ), while the strong holes remain on  $\text{WO}_3$  to oxidize  $\text{H}_2\text{O}$  or  $\text{OH}^-$  into  $\cdot\text{OH}$ . This mechanism prolongs the lifetime of the strong carriers to the microsecond-millisecond ( $\mu\text{s}$ – $\text{ms}$ ) range and suppresses undesired bulk recombination, consistent with the band-edge shifts observed in DRS and the lower  $R_{\text{ct}}$  measured in EIS (Fig. 6), thereby supporting efficient charge separation at the Ti-W interface and enhanced photocatalytic oxidation of pollutants. (2020; Iqbal *et al.* 2021; Park *et al.* 2016; Serpone and Emeline 2012; Sotelo-Vazquez *et al.* 2017).



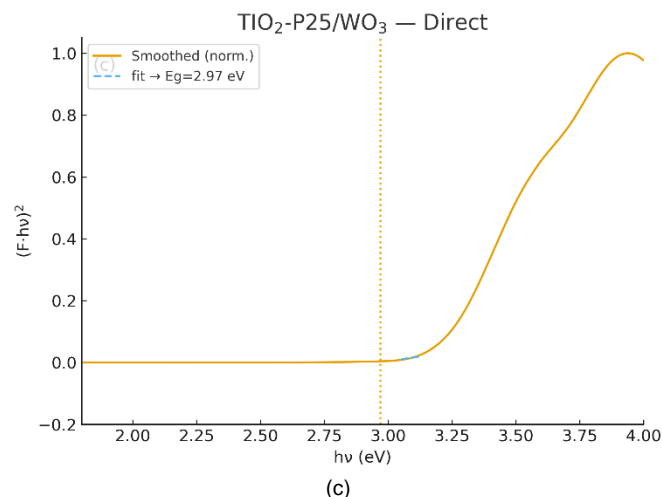


**Fig. 5.** Tauc plots from UV–Vis DRS of (a)  $\text{TiO}_2$ -P25, (b)  $\text{WO}_3$ , and (c)  $\text{TiO}_2$ -P25/ $\text{WO}_3$ . Band gaps estimated at 3.21, 2.53, and 2.97 eV, respectively, align with reported ranges.

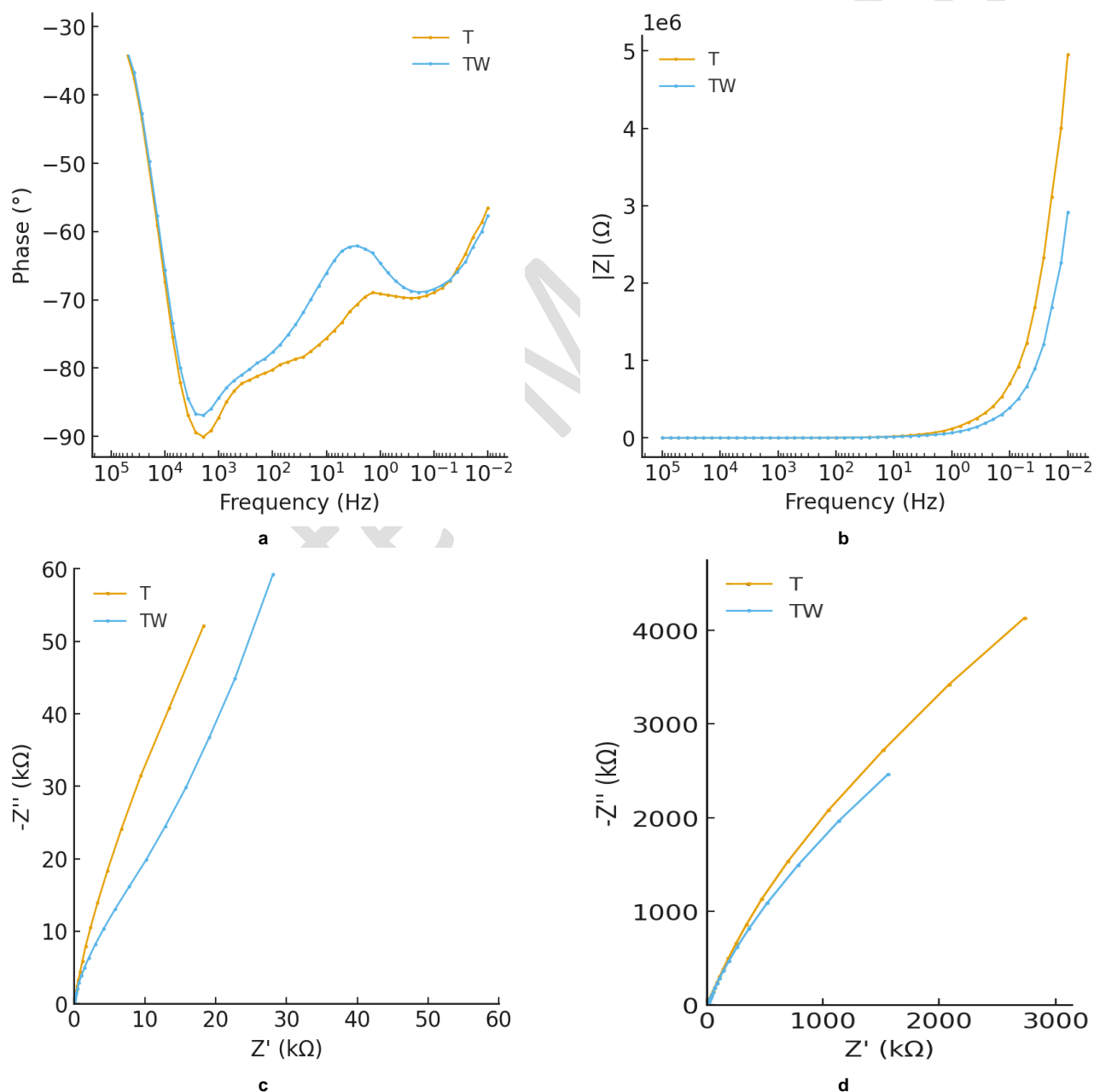


**Fig. 6.** Electrochemical impedance spectra (EIS) of  $\text{TiO}_2$ -P25 (T) and  $\text{TiO}_2$ -P25/ $\text{WO}_3$  (TW). (a) Bode phase and (b) Bode  $|Z|$  plots show reduced impedance for TW. (c, d) Nyquist plots reveal smaller arc and lower  $R_{ct}$  for TW, indicating efficient charge separation at the Ti–W heterojunction.

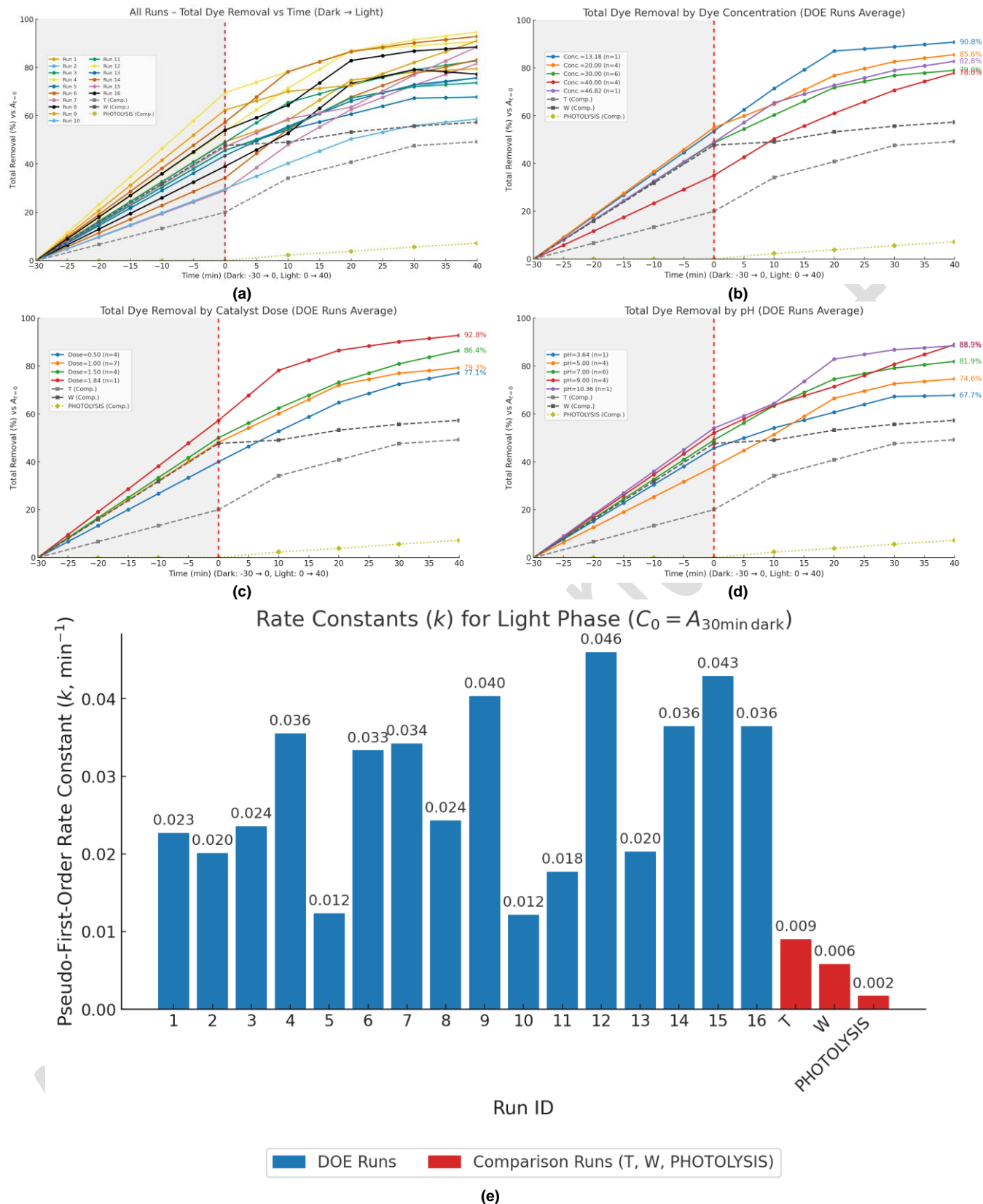


**Fig. 7.** Photocatalytic MB degradation under sunlight. (a) Time-resolved removal for  $\text{TiO}_2\text{-P25}$ ,  $\text{WO}_3$ , TW, and controls. (b) Effect of pH, with optimum near 9. (c) Dependence on catalyst dose. (d) Effect of initial MB concentration. (e) Pseudo-first-order kinetics, showing  $k_{\text{app}}(\text{TW}) > k_{\text{app}}(\text{T}) \gg k_{\text{app}}(\text{photolysis})$ .

For both the dark-equilibration step and the subsequent photocatalytic kinetics,  $\zeta$ -potential is decisive. At the working pH (above  $\text{pH}_{\text{pzc}}$ ), TW exhibits a moderately negative  $\zeta$ -potential that electrostatically attracts cationic MB, thereby increasing its interfacial concentration before illumination (Khan *et al.* 2022). In parallel, the same negative surface enriches ROS precursors ( $\text{O}_2$ ,  $\text{OH}^-$ ) near the catalyst, biasing the microenvironment toward efficient radical generation (Bollinger *et al.* 2025). Consequently, the apparent rate depends not only on the bulk MB concentration but also on charge-

mediated interfacial enrichment, which accelerates consumption of photogenerated  $^{\bullet}\text{O}_2^-$  and  $^{\bullet}\text{OH}$ . Notably, this adsorption-charge interplay mirrors the CCD-optimized pH-dose- $C_0$  response surface: conditions that render  $\zeta$  more negative consistently coincide with higher activity (Khan *et al.* 2022). Fig. 9 sketches the  $\zeta$ -potential distribution of TW (mean  $\approx -22$  mV), within the borderline-stable regime and favorable for cationic MB uptake.



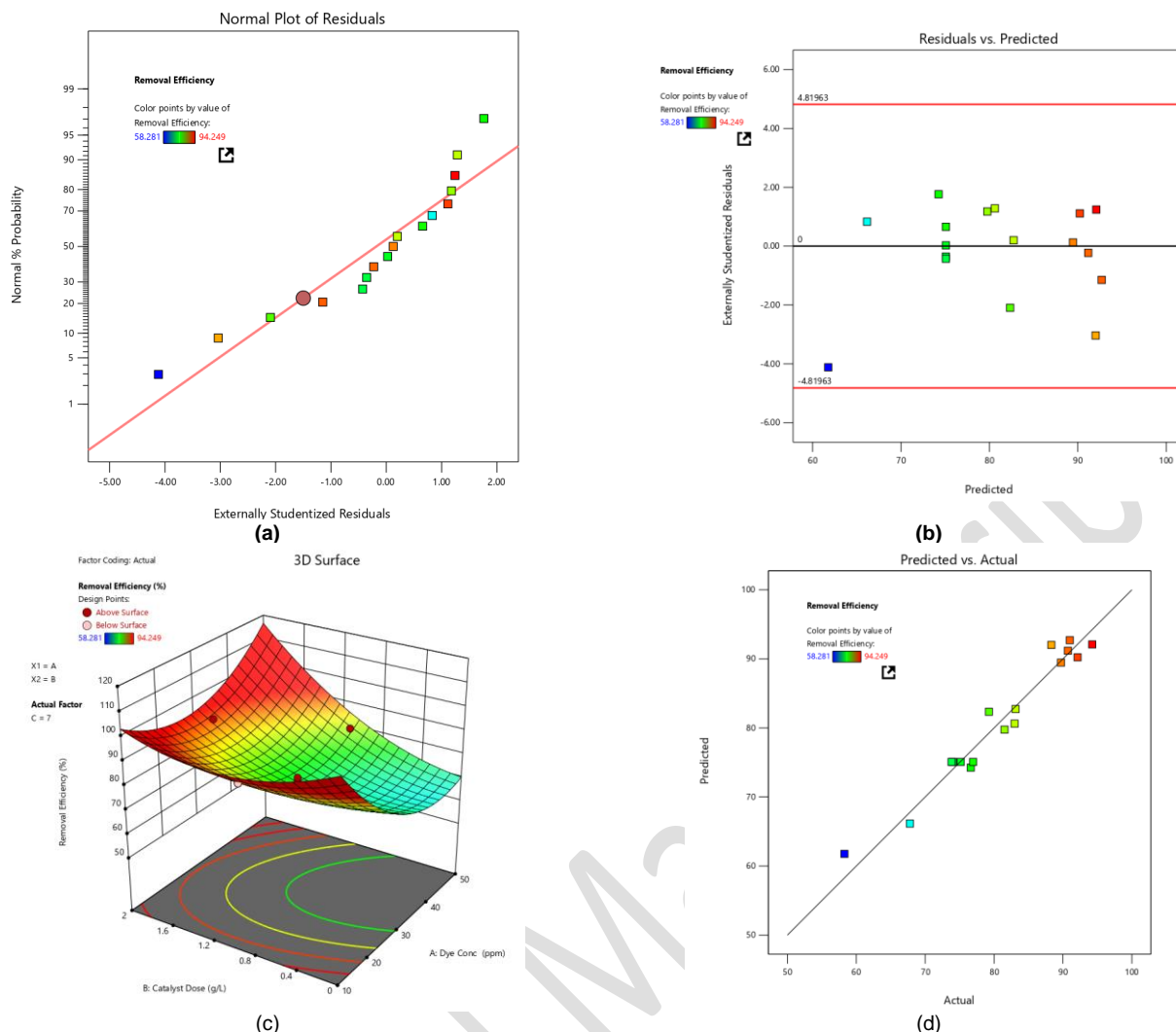
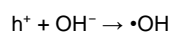
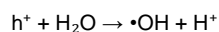
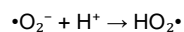
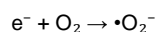


**Fig. 8.** (a) DOE model diagnostics and response surfaces, (b) normal probability plot, (c) residuals vs. predicted values, (d) 3D response surface (A, B at fixed pH) showing curvature and optimum, (e) predicted vs. actual parity plot confirming strong predictivity.

**Table 1.** Central composite design (CCD) matrix with experimental runs showing the effects of initial dye concentration (mg/L), catalyst dose (g/L), and pH on removal efficiency (%).

Run	pH	Catalysis dose	Dye concentration	Removal, %
1	5	1.5	20	79.256
2	7	1	30	75.155
3	7	1	46.82	82.978
4	7	1	13.18	90.716
5	3.64	1	30	67.786
6	5	1.5	40	83.123
7	9	0.5	40	81.522
8	5	0.5	20	76.62
9	9	0.5	20	90.99
10	5	0.5	40	58.281
11	7	1	30	73.832
12	9	1.5	20	94.249
13	7	1	30	74.04
14	7	1.84	30	92.123
15	9	1.5	40	88.32
16	10.36	1	30	89.723
17	7	1	30	76.958

FTIR and Raman spectra of TW overlap without new bands or phonon modes, indicating that no additional interfacial bonds formed; nevertheless, the close physical contact permits short-range electronic coupling sufficient to facilitate interfacial charge transport, in agreement with EIS (Bhavani *et al.* 2022; Boga *et al.* 2018).



Taken together, these results support the conclusion that TW establishes a physically contacted heterointerface through which photogenerated electrons are funneled into the  $TiO_2$ -P25 conduction band while holes remain in the  $WO_3$  valence band, thereby activating  $O_2$  reduction and  $H_2O/OH^-$  oxidation. As shown schematically in Fig. 10, the interfacial charge separation achieved under mild, additive-free conditions provides a stable pathway for continuous ROS generation.

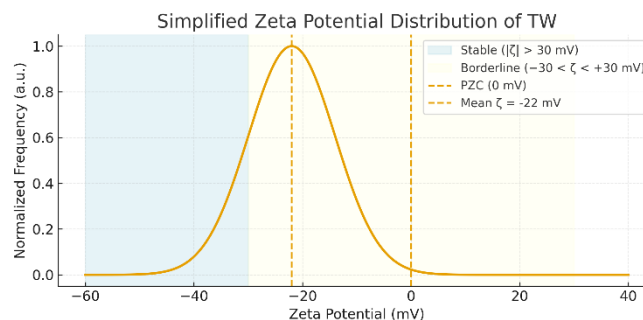


**Fig. 9.** Simplified  $\zeta$ -potential distribution of TW. The mean  $\zeta$  (-22 mV, dashed line) lies within the borderline regime ( $-30 < \zeta < +30$  mV), close to the PZC (0 mV), indicating moderate colloidal stability and favorable attraction of cationic MB.

This process directly accounts for the strong photocatalytic performance of TW and is in good agreement with earlier studies on  $WO_3/TiO_2$ -P25 composites, which reported similar electron-hole partitioning and radical-driven pathways (Boga *et al.* 2018; Gao *et al.* 2017; L. Ernawatia *et al.* 2019; Tran *et al.* 2019; Yan *et al.* 2020).

### 3.5. Catalyst stability and reusability

The long-term stability and reusability of the TW composite were evaluated through four consecutive photocatalytic cycles under the optimized conditions.

**Table 2.** Analysis of variance (ANOVA) for the quadratic response surface model of removal efficiency, showing the significance of linear, interaction, and quadratic terms. The model is statistically significant ( $p = 0.0007$ ) with a non-significant lack of fit ( $p = 0.0614$ ).

Source	Sum of squares	df	Mean square	F-value	p-value	
Model	1424.93	9	158.33	15.81	0.0007	significant
A-Dye Conc	134.65	1	134.65	13.44	0.0080	
B-Catalyst Dose	231.54	1	231.54	23.12	0.0019	
C-pH	656.63	1	656.63	65.56	< 0.0001	
AB	82.85	1	82.85	8.27	0.0238	
AC	0.1070	1	0.1070	0.0107	0.9206	
BC	37.94	1	37.94	3.79	0.0927	
A <sup>2</sup>	176.95	1	176.95	17.67	0.0040	
B <sup>2</sup>	42.70	1	42.70	4.26	0.0778	
C <sup>2</sup>	11.26	1	11.26	1.12	0.3242	
Residual	70.11	7	10.02			
Lack of Fit	63.96	4	15.99	7.81	0.0614	not significant
Pure Error	6.14	3	2.05			
Cor Total	1495.03	16				

As shown in Fig. 11, the degradation efficiency of Methylene Blue decreased by only about 9% after the fourth cycle, demonstrating excellent recyclability and structural integrity. This performance stability is attributed to the chemical robustness of the  $\text{TiO}_2\text{-P25/WO}_3$  heterojunction and the intimate interfacial contact achieved via the mild sonochemical process. The observed results are consistent with previously reported  $\text{TiO}_2\text{/WO}_3$  systems, confirming that the green-synthesized TW catalyst is suitable for long-term real sunlight-driven photocatalytic applications. (Bitaraf and Amoozadeh 2020; Jiang *et al.* 2021).

### 3.6. Comparison of photocatalytic performance

To contextualize the efficiency achieved by the TW composite, its photocatalytic performance was benchmarked against comparable  $\text{TiO}_2\text{/WO}_3$  heterostructures and similar systems reported in the literature (Table 3). The comparison highlights two primary advantages of the present work:

(i) Simplicity and Green Chemistry: The TW catalyst was fabricated through an exceptionally fast (10 min), additive-free, aqueous sonochemical route. This synthesis is markedly simpler and more energy-efficient than conventional methods involving high-temperature

calcination, multi-step hydrothermal procedures (Hou and Hao 2021; L. Ernawatia *et al.* 2019), or covalent grafting (Bitaraf and Amoozadeh 2020).

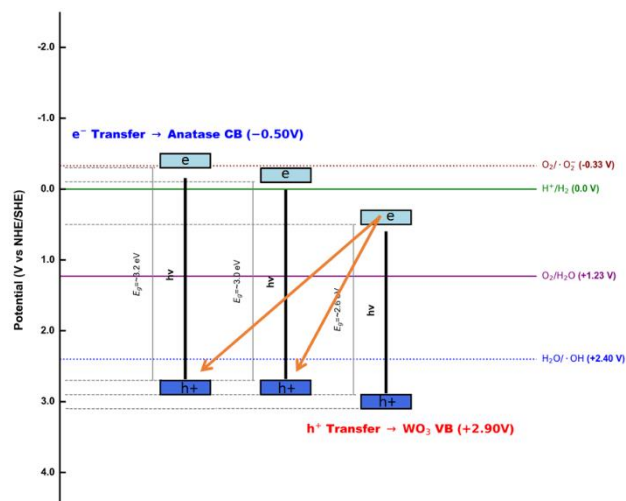


**Fig. 10.** Interfacial charge transfer and ROS generation in  $\text{TiO}_2\text{-P25/WO}_3$  under sunlight (z-scheme).

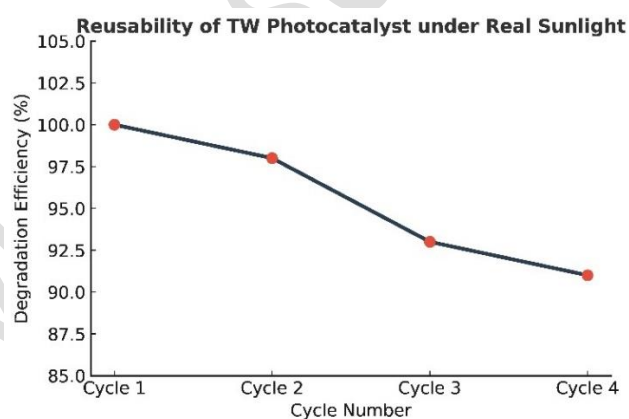


**Fig. 11.** Reusability performance of the green-synthesized  $\text{TiO}_2\text{-P25/WO}_3$  (TW) photocatalyst under real sunlight irradiation.

(ii) High Efficiency under Real Sunlight: Despite its minimal and environmentally benign synthesis process, the TW composite exhibits comparable or superior kinetic performance toward target pollutants under the less-controlled yet practical conditions of real sunlight exposure. This robust photocatalytic response under natural illumination underscores the potential of this scalable and sustainable approach for cost-effective environmental remediation.

**Table 3.** Comparison of the photocatalytic performance of the composite with literature-reported heterostructures.

Catalyst	$\text{WO}_3$ , wt%	Synthesis method	Light source	Pollutant target	$k_{\text{app}}$ ( $\text{min}^{-1} \times 10^{-3}$ )	Reference
TW (This Work)	30	Sonochemical (10 min, additive-free)	Real sunlight	MB	42	This work
$\text{WO}_3\text{/TiO}_2$ NRs	–	Hydrothermal	Visible light	MB	11.2	(Jiang <i>et al.</i> 2021)
$\text{WO}_3\text{/F-TiO}_2$	5	Hydrothermal	Visible light	MB	10.3	(Hou and Hao 2021)
$\text{WO}_3\text{/TiO}_2$ Nanocomposite	25	Hydrothermal / Wet chemical	Visible light	MB	17.5	(L. Ernawatia <i>et al.</i> 2019)
$\text{TiO}_2\text{/WO}_3$	10	Solvothermal	Visible light	RhB	2.4	(Gao <i>et al.</i> 2017)

### 4. Conclusions

In summary, we demonstrated an organic-solvent-free, water-based, one-pot sonication-drying route to a physically contacted  $\text{TiO}_2\text{-P25/WO}_3$  photocatalyst that delivers robust sunlight activity. The results show that a green, straightforward fabrication can coexist with efficient charge separation and steady ROS generation under real-world illumination. This approach offers a practical alternative to multi-step

wet-chemistry routes—simple, cost-effective, and safer to handle—as highlighted in recent overviews (Khatami and Iravani 2021). The mild workflow also facilitates scale-up (no complex reactors or solvent recovery) and leverages the availability and eco-compatibility of  $\text{TiO}_2\text{-P25}$  and  $\text{WO}_3$ . Thus, our method improves sustainability without sacrificing performance, supporting pilot- to plant-level translation. (Li *et al.* 2025; Thambiliyagodage 2021) and can be extended to other oxide pairings where physical contact suffices.

## Data Availability Statement

Data will be made available on request.

## Author Contribution

Mahdi Jamshidi: Carried out the experimental work, performed data analysis, and prepared the first draft of the manuscript. A. Amoozadeh conceived and supervised the study, contributed to the interpretation of the results, and critically revised and edited the manuscript.

Both authors reviewed and approved the final manuscript.

## Acknowledgments

The authors gratefully thank Faculty of Chemistry of Semnan University, Semnan, Iran, for supporting this work.

## Conflict of Interest

The authors declare that they have no known competing financial interests or personal relationships that could have appeared to influence the work reported in this paper.

## References

- Ahmadpour, N. *et al.* (2024) 'Design and optimization of TiO<sub>2</sub>-based photocatalysts for efficient removal of pharmaceutical pollutants in water: Recent developments and challenges', *Journal of Water Process Engineering*, 57, p. 104597. doi: <https://doi.org/10.1016/j.jwpe.2023.104597>
- Al-Ghamdi, A.A. *et al.* (2025) 'An easy and single-step biosynthesis of WO<sub>3</sub> with high photocatalytic degradation activity for dye degradation', *Nanomaterials (Basel)*, 15, p. 1036. doi: <https://doi.org/10.3390/nano15131036>
- Anastas, P.T., and Warner, J.C. (2000) *Green chemistry*. New York: Oxford University Press.
- Azeez, F. *et al.* (2018) 'The effect of surface charge on photocatalytic degradation of methylene blue dye using chargeable titania nanoparticles', *Scientific Reports*, 8, p. 7104. doi: <https://doi.org/10.1038/s41598-018-25673-5>
- Balu, S. *et al.* (2024) 'Advanced photocatalytic materials based degradation of micropollutants and their use in hydrogen production - a review', *RSC Advances*, 14, pp. 14392-14424. doi: <https://doi.org/10.1039/d4ra01307g>
- Bhavani, P. *et al.* (2022) 'Recent advances in wide solar spectrum active WO<sub>3</sub>-based photocatalysts for energy and environmental applications', *Catalysis Reviews*, 65, pp. 1521-1566. doi: <https://doi.org/10.1080/01614940.2022.2038472>
- Bitaraf, M. and Amoozadeh, A. (2020) 'The first report of covalently grafted semiconductors; n-TiO<sub>2</sub>-P25@ECH@WO<sub>3</sub> as a new, efficient, robust and visible-light-responsive photocatalyst', *Journal of Chemical Technology & Biotechnology*, 96, pp. 963-970. doi: <https://doi.org/10.1002/jctb.6605>
- Boga, B. *et al.* (2018) 'Detailed spectroscopic and structural analysis of TiO<sub>2</sub>/WO<sub>3</sub> composite semiconductors', *Journal of Spectroscopy*, 2018, pp. 1-7. doi: <https://doi.org/10.1155/2018/6260458>
- Bollinger, J.-C. *et al.* (2025) 'Molecular properties of methylene blue, a common probe in sorption and degradation studies: A review', *Environmental Chemistry Letters*, 23, pp. 1403-1424. doi: <https://doi.org/10.1007/s10311-025-01856-1>
- Brandl, F. *et al.* (2020) 'Consecutive photoinduced electron transfer (conpet): The mechanism of the photocatalyst rhodamine 6g', *Chemistry*, 26, pp. 7946-7954. doi: <https://doi.org/10.1002/chem.201905167>
- Cheng, K. *et al.* (2024) 'Mixed Metal Oxide W-TiO<sub>2</sub> Nanopowder for Environmental Process: Synergy of Adsorption and Photocatalysis', *Nanomaterials (Basel)*, 14, p. 765. doi: <https://doi.org/10.3390/nano14090765>
- Dolatyari, M. *et al.* (2024) 'Core/Shell ZnO/TiO<sub>2</sub>, SiO<sub>2</sub>/TiO<sub>2</sub>, Al<sub>2</sub>O<sub>3</sub>/TiO<sub>2</sub>, and Al<sub>1.9</sub>Co<sub>0.1</sub>O<sub>3</sub>/TiO<sub>2</sub> Nanoparticles for the Photodecomposition of Brilliant Blue E-4BA', *Inorganics*, 12, p. 281. doi: <https://doi.org/10.3390/inorganics12110281>
- Farghaly, A. *et al.* (2024) 'Synergistic photocatalytic degradation of methylene blue using TiO<sub>2</sub> composites with activated carbon and reduced graphene oxide: a kinetic and mechanistic study', *Applied Water Science*, 14, p. 228. doi: <https://doi.org/10.1007/s13201-024-02286-0>
- Gao, L. *et al.* (2017) 'Preparation of heterostructured WO<sub>3</sub>/TiO<sub>2</sub> catalysts from wood fibers and its versatile photodegradation abilities', *Scientific Reports*, 7, p. 1102. doi: <https://doi.org/10.1038/s41598-017-01244-y>
- Ghiloufi, M. *et al.* (2024) 'Photocatalytic activity and electrochemical properties of a ternary-based-TiO<sub>2</sub> nanocomposite', *Inorganic and Nano-Metal Chemistry*, 55, pp. 678-691. doi: <https://doi.org/10.1080/24701556.2024.2354485>
- Glowniak, S. *et al.* (2023) 'Recent developments in sonochemical synthesis of nanoporous materials', *Molecules*, 28, p. 2639. doi: <https://doi.org/10.3390/molecules28062639>
- González Rodríguez, L.M. *et al.* (2020) 'Synthesis, characterization and photocatalytic activity evaluation of WO<sub>3</sub>, TiO<sub>2</sub> and WO<sub>3</sub>/TiO<sub>2</sub> supported on zeolite faujasite', *International Journal of Chemical Reactor Engineering*, 18, p. 20200095. doi: <https://doi.org/10.1515/ijcre-2020-0095>
- Gonzalez, S. and Jaramillo-Fierro, X. (2025) 'Density functional theory study of methylene blue demethylation as a key step in degradation mediated by reactive oxygen species', *International Journal of Molecular Sciences*, 26, p. 1756. doi: <https://doi.org/10.3390/ijms26041756>
- Hosseini, S., Amoozadeh, A. and Akbarzadeh, Y. (2019) 'Nano-WO<sub>3</sub>-SO<sub>3</sub>H as a New Photocatalyst Insight Through Covalently Grafted Brønsted Acid: Highly Efficient Selective Oxidation of Benzyl Alcohols to Aldehydes', *Photochemistry and Photobiology*, 95, pp. 1320-30, doi: <https://doi.org/10.1111/php.13142>
- Hou, C. and Hao, J. (2021) 'A three-dimensional nano-network WO<sub>3</sub>/F-TiO<sub>2</sub>{001} heterojunction constructed with OH-TiOF<sub>2</sub> as the precursor and its efficient degradation of methylene blue', *RSC Advances*, 11, pp. 26063-26072. doi: <https://doi.org/10.1039/d1ra04809k>
- Iqbal, A. *et al.* (2021) 'Charge Transport Phenomena in Heterojunction Photocatalysts: The WO<sub>3</sub>/TiO<sub>2</sub> System as an Archetypical Model', *ACS Applied Materials & Interfaces*, 13, pp. 9781-9793. doi: <https://doi.org/10.1021/acsami.0c19692>
- Jiang, L. *et al.* (2021) 'Oxygen-Deficient WO<sub>3</sub>/TiO<sub>2</sub>/CC Nanorod Arrays for Visible-Light Photocatalytic Degradation of Methylene Blue', *Catalysts*, 11, p. 1349. doi: <https://doi.org/10.3390/catal11111349>
- Kalaycioglu, Z. *et al.* (2023) 'Efficient photocatalytic degradation of methylene blue dye from aqueous solution with cerium oxide nanoparticles and graphene oxide-doped polyacrylamide', *ACS Omega*, 8, pp. 13004-13015. doi: <https://doi.org/10.1021/acsomega.3c00198>
- Kanafin, Y.N. *et al.* (2025) 'A review on WO<sub>3</sub> photocatalysis used for wastewater treatment and pesticide degradation', *Heliyon*, 11, p. e40788. doi: <https://doi.org/10.1016/j.heliyon.2024.e40788>
- Khan, I. *et al.* (2022) 'Review on methylene blue: Its properties, uses, toxicity and photodegradation', *Water*, 14, p. 242. doi: <https://doi.org/10.3390/w14020242>
- Khan, S., *et al.* (2024) 'Photocatalytic dye degradation from textile wastewater: A review', *ACS Omega*, 9, pp. 21751-21767. doi: <https://doi.org/10.1021/acsomega.4c00887>
- Khatami, M., and Iravani, S. (2021) 'Green and eco-friendly synthesis of nanophotocatalysts: An overview', *Comments on Inorganic Chemistry*, 41, pp. 133-87, doi: <https://doi.org/10.1080/02603594.2021.1895127>
- Kulkarni, S.N. *et al.* (2025) 'Recent trends in TiO<sub>2</sub> focused s-scheme heterojunctions for photocatalytic innovations: A comprehensive analysis', *Journal of Alloys and Compounds*, 1016, pp., doi: <https://doi.org/10.1016/j.jallcom.2025.178876>
- Ernawatia, L. *et al.* (2019) 'Mesoporous WO<sub>3</sub>/TiO<sub>2</sub> nanocomposites photocatalyst for rapid degradation of methylene blue in aqueous medium', *International Journal of Engineering*, 32, pp. 1345-1352. doi: <https://doi.org/10.5829/ije.2019.32.10a.02>
- Li, Y. *et al.* (2025) 'Multifunctional non-stoichiometric tungsten oxides: Synthesis, properties and application', *Journal of Power Sources*, 631, p. 236222. doi: <https://doi.org/10.1016/j.jpowsour.2025.236222>

- Liu, Y. *et al.* (2020) 'An in situ assembled WO<sub>3</sub>-TiO<sub>2</sub> vertical heterojunction for enhanced Z-scheme photocatalytic activity', *Nanoscale*, 12, pp. 8775-84. doi: <https://doi.org/10.1039/d0nr01611j>
- Matinise, N. *et al.* (2025) 'Enhanced photocatalytic degradation of methylene blue using zinc vanadate nanomaterials with structural and electrochemical properties', *Scientific Reports*, 15, p. 26333. doi: <https://doi.org/10.1038/s41598-025-11418-8>
- Min, N. *et al.* (2025) 'Carbon, hydrogen, nitrogen and chlorine isotope fractionation during 3-chloroaniline transformation in aqueous environments by direct photolysis, TiO<sub>2</sub> photocatalysis and hydrolysis', *Water Research*, 273, p. 122956, doi: <https://doi.org/10.1016/j.watres.2024.122956>
- Moghni, N. *et al.* (2022) 'Enhanced photocatalytic activity of TiO<sub>2</sub>/WO<sub>3</sub> nanocomposite from sonochemical-microwave assisted synthesis for the photodegradation of ciprofloxacin and oxytetracycline antibiotics under uv and sunlight', *Journal of Photochemistry and Photobiology A: Chemistry*, 428, pp. 113848. doi: <https://doi.org/10.1016/j.jphotochem.2022.113848>
- Nguyen, B.C. *et al.* (2024) 'Advanced cellulose-based hydrogel TiO<sub>2</sub> catalyst composites for efficient photocatalytic degradation of organic dye methylene blue', *Scientific Reports*, 14, p. 10935. doi: <https://doi.org/10.1038/s41598-024-61724-w>
- Nik Ramli Nik F.N.A. *et al.* (2024) 'Photodegradation of Methylene Blue over WO<sub>3</sub>/TiO<sub>2</sub> Composites under Low UV-C Irradiation and Scavenger Analysis', *Malaysian Journal of Chemistry*, 26, pp. 358-69. doi: <https://doi.org/10.55373/mjchem.v26i5.358>
- Park, H. *et al.* (2016) 'Photoinduced charge transfer processes in solar photocatalysis based on modified TiO<sub>2</sub>', *Energy & Environmental Science*, 9, pp. 411-33. doi: <https://doi.org/10.1039/c5ee02575c>
- Serpone, N., and Emeline, A.V. (2012) 'Semiconductor photocatalysis - past, present, and future outlook', *Journal of Physical Chemistry Letters*, 3, pp. 673-6777. doi: <https://doi.org/10.1021/jz300071j>
- Serra-Pérez, E. *et al.* (2024) 'Influence of the surface structure of the TiO<sub>2</sub> support on the properties of the Au/TiO<sub>2</sub> photocatalyst for water treatment under visible light', *Catalysis Today*, 437, p. 114764. doi: <https://doi.org/10.1016/j.cattod.2024.114764>
- Sharifiyan, M.S., Fattah-alhosseini, A. and Karbasi, M. (2023) 'Photocatalytic evaluation of hierarchical TiO<sub>2</sub>/WO<sub>3</sub> hybrid coating created by peo/hydrothermal method', *Applied Surface Science Advances*, 18, p. 100541. doi: <https://doi.org/10.1016/j.apsadv.2023.100541>
- Shoaib, M., *et al.* (2023) 'Dual s-scheme heterojunction cds/tio(2)/g-c(3)n(4) photocatalyst for hydrogen production and dye degradation applications', *ACS Omega*, 8, pp. 43139-50, doi: <https://doi.org/10.1021/acsomega.3c06759>
- Sotelo-Vazquez, C. *et al.* (2017) 'Evidence and effect of photogenerated charge transfer for enhanced photocatalysis in WO<sub>3</sub> /TiO<sub>2</sub> heterojunction films: A computational and experimental study', *Advanced Functional Materials*, 27, pp. 1605413. doi: <https://doi.org/10.1002/adfm.201605413>
- Thambiliyagodage, C. (2021) 'Activity enhanced TiO<sub>2</sub> nanomaterials for photodegradation of dyes - a review', *Environmental Nanotechnology, Monitoring & Management* 16, p. 100592. doi: <https://doi.org/10.1016/j.enmm.2021.100592>
- Tran, K. *et al.* (2019) 'Evidence for moire excitons in van der waals heterostructures', *Nature*, 567, pp. 71-75. doi: <https://doi.org/10.1038/s41586-019-0975-z>
- Vasiljevic, Z.Z. *et al.* (2020) 'Photocatalytic degradation of methylene blue under natural sunlight using iron titanate nanoparticles prepared by a modified sol-gel method', *Royal Society Open Science*, 7, p. 200708. doi: <https://doi.org/10.1098/rsos.200708>
- Yan, Y. *et al.* (2020) 'Van der waals heterojunctions for catalysis', *Materials Today Advances*, 6, p. 100059. doi: <https://doi.org/10.1016/j.mtadv.2020.100059>
- Yang, Y. *et al.* (2025) 'Hollow flower-like WO<sub>3</sub>@TiO<sub>2</sub> heterojunction microspheres for the photocatalytic degradation of rhodamine B and tetracycline', *RSC Advances*, 15, pp. 12629-12644. doi: <https://doi.org/10.1039/d5ra01412c>
- Yin, X., Liu, L. and Ai, F. (2021) 'Enhanced Photocatalytic Degradation of Methylene Blue by WO<sub>3</sub> Nanoparticles Under NIR Light irradiation', *Frontiers in Chemistry*, 9, p. 683765. doi: <https://doi.org/10.3389/fchem.2021.683765>